Journal of Power Sources 196 (2011) 4143–4151

Contents lists available at ScienceDirect

Journal of Power Sources

journal homepage: www.elsevier.com/locate/jpowsour

Cubic titanium dioxide photoanode for dye-sensitized solar cells

Jinho Chae, Misook Kang*

Department of Chemistry, College of Science, Yeungnam University, Gyeongsan, Gyeongbuk 712-749, Republic of Korea

ARTICLE INFO

Article history:
Received 30 September 2010
Received in revised form 7 December 2010
Accepted 12 December 2010
Available online 18 January 2011

Keywords:
Cubic titanium
Amine species additives
Dye-sensitized solar cell
Photovoltaic efficiency
Electrostatic force microscopy
Impedance

ABSTRACT

Following from the recently evolved concept of significantly improving the photovoltaic efficiency in dye-sensitized solar cells (DSSCs) by reducing the loss of electrons on the spherical surface of titanium dioxide, this study examines the synthesis of cubic TiO_2 with a special morphology to overcome this electron loss and investigates its application to DSSCs. Cubic TiO_2 is synthesized by an advanced rapid hydrothermal method, with the addition of an amine species additive. Transmission electron microscopy (TEM) images confirm the cubic shape of the TiO_2 particles with a diameter less than 5–10 nm. Using N719 dye under illumination with 100 mW cm^{-2} simulated sunlight, the application of cubic TiO_2 to DSSCs affords an energy conversion efficiency of approximately 9.77% (4.0-μm thick TiO_2 film), which is considerably enhanced compared with that achieved using a commercial, spherical TiO_2. Electrostatic force microscopy (EFM) and impedance analyses reveal that the electrons are transferred more rapidly to the surface of a cubic TiO_2 film than on a spherical TiO_2 film.

1. Introduction

Dye-sensitized solar cells (DSSCs) have been investigated extensively due to their inherent attractive advantages of low cost, less toxic manufacturing, easy scale-up, light weight, and use of flexible panels compared with silicon and inorganic, thin-film solar cells with conventional p–n junction devices [1–5]. DSSCs consist of a fluorine-doped SnO_2 electrode, titanium dioxide (TiO_2) film, a sensitizing dye, electrolyte, and a counter electrode. When a light photon is absorbed by a dye molecule, it excites the electrons in the highest occupied molecular orbital (HOMO) to an electronically excited state, i.e., the lowest unoccupied molecular orbital (LUMO). The excited dye molecule injects an electron into the conducting band of the TiO_2 film, and the oxidized dye is restored by electron donation from reducing ions in the electrolyte, usually an organic solvent containing a redox system. The donated electron is in turn regenerated by the reduction of conjugated ions in the electrolyte. The circuit is completed by electron migration through an external load.

Nanocrystalline TiO_2 materials have been studied extensively because of their interesting physical and chemical properties: in particular their redox reaction surface. Following the first report of the DSSC principle by Graetzel [6], the cell has been rapidly developed with pure [7–11] or metal-incorporated TiO_2 [12–14]. Additionally, mesoporous TiO_2 has an optical efficiency that is approximately 0.5–1.0% higher than that of the existing nanoparticles [15–18]. Lin et al. [19] reported that compared with TiO_2 nanoparticles/Ti-based DSSCs, conical-shaped anodic TiO_2-nanotubes/Ti-based DSSCs showed enhanced light-harvesting efficiency, rapid electron-transport rate, prolonged electron lifetime, and reduced dark current – properties lead to an efficiency increment of 30%. Other semiconducting materials, such as nano-sized Sn and Zn oxides with a slightly higher band gap than pure TiO_2, which can improve the electron donating/accepting capability between the semiconductor and the LUMO energy levels of the dye, have been examined, but some performance degradation has been reported [20,21]. Therefore, the search for superior metal oxides will continue.

In DSSC research, the bulk morphology is based on the type of additive. Wu et al. [22] reported attaining a 6.2% photoelectric conversion efficiency from a DSSC with rod-like anatase, compared with a 5.4% efficiency from a DSSC with ball-like anatase. Lee et al. [23] found that the open-circuit voltage (V_{oc}) of the DSSC increased as the weight percentage of the Ti nanotube was increased to an optimum value of about 5.0 wt%. Park et al. [24] also reported increased short-circuit photocurrent (J_{sc}) and open-circuit photo voltage, and significantly improved the conversion efficiency in a cell using plant oil binders. Lee et al. [25] examined the influence of different TiO_2 morphologies and solvents on the photovoltaic performance of DSSCs. The authors attributed this influence to the effect solvents on the bulk morphology of the TiO_2 thick film. Zhang et al. [26] applied different film thicknesses to DSSC and obtained an overall light-to-electricity conversion efficiency of 2.91% at a thickness of 2.0 μm. Remarkably, no structural morphology study has yet been reported for TiO_2. In the present study, therefore, an attempt is made to control the TiO_2 morphology in the synthesis

* Corresponding author. Tel.: +82 53 810 2363; fax: +82 53 815 5412.
E-mail address: mskang@ynu.ac.kr (M. Kang).

0378-7753/$ – see front matter © 2011 Elsevier B.V. All rights reserved.
doi:10.1016/j.jpowsour.2010.12.109

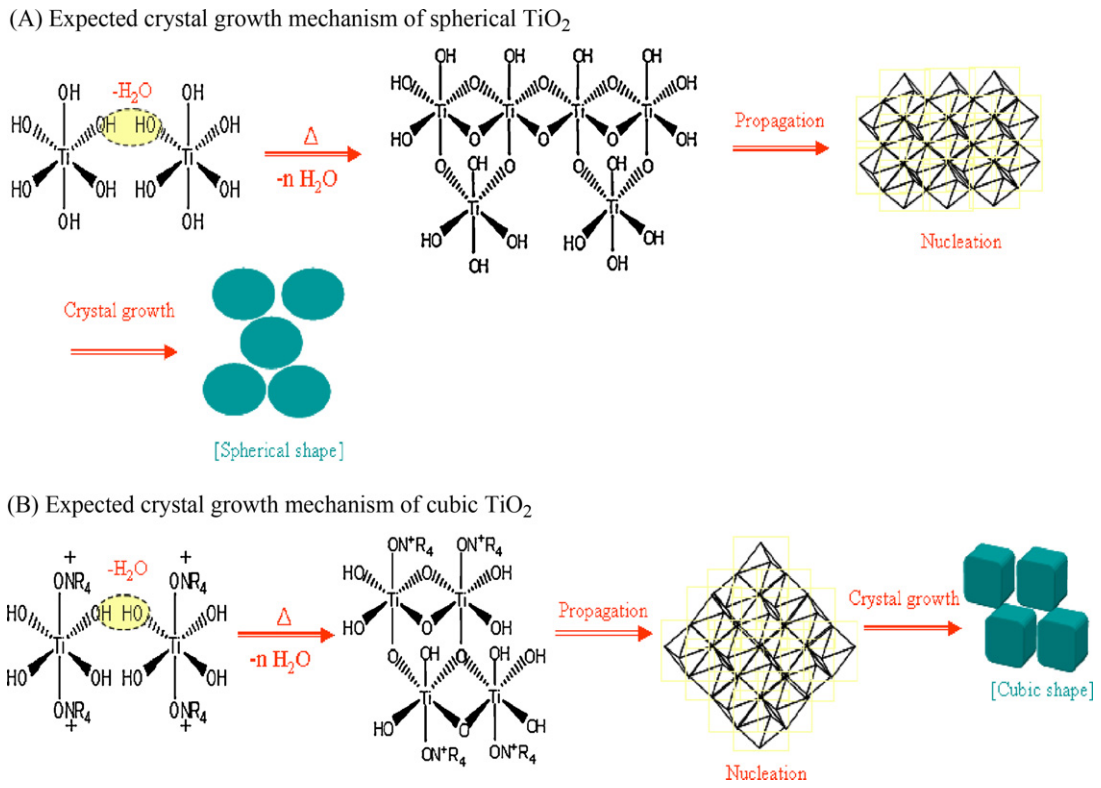

Fig. 1. Expected crystal growth mechanism of (A) spherical and (B) cubic TiO_2 fabricated by hydrothermal method.

steps by focusing on its electron transfer ability. To enhance the photovoltaic efficiency, the electrons transferred from the LUMO of the dye molecules should be easily accepted and donated on the external surface of the TiO_2 film. The loss of electrons on the spherical surface of the TiO_2 nanoparticles limits this enhancement. A cubic TiO_2 film that has been well arranged by self assembly is expected to facilitate the rapid movement of electrons on its surface, and their subsequent return to a fluorine-doped tin oxide-conducting electrode without electron loss, thereby increasing the energy conversion efficiency.

Therefore, this study focuses on the preparation of nano-structured, cubic TiO_2 films for DSSCs to enhance the photovoltaic efficiency. The cubic TiO_2 is synthesized using an advanced, rapid hydrothermal method with special amine additives, and then characterized by X-ray diffraction (XRD), transmission electron microscopy (TEM), FT-Raman spectroscopy, X-ray photon spectroscopy (XPS), photoluminescence (PL), UV–visible spectra, and electrostatic force microscopy (EFM) analysis. The photovoltaic performance of the cubic TiO_2/dye (N719) solar cell is evaluated from the overall conversion efficiency, fill factor (FF), V_{oc} and J_{sc}. Additionally, the efficiency is compared with that of a spherical TiO_2 sample prepared by a conventional hydrothermal method.

2. Experimental

2.1. Preparation of cubic TiO_2

Nano-structured, cubic TiO_2 was prepared using an advanced rapid hydrothermal method [27,28]. To prepare the sol mixture, 1.0 mol titanium tetraisopropoxide (TTIP, 99.95%, Junsei Chemical, Tokyo, Japan) was added as the titanium precursor to 1.0 L of distilled water as the solvent. To depress the condensation reaction at the terminal groups, 0.1 mol of tetraethyl ammonium hydroxide as a blocking template was added to the former solution, which was then stirred for 2 h. During this stirring, the concentration of tetraethyl ammonium hydroxide had to be controlled for complete blocking of the terminal groups of titanium. The TTIP and template were hydrolyzed via the OH group during thermal treatment at 200 °C for 1 h with about 10.0 atm under an nitrogen environment. As shown in Fig. 1, the condensation reaction with H_2O elimination generally induces a combination between each titanium hydroxide. During this reaction, the condensation reaction continues in the absence of any blocking molecules like amine groups. The resulting nucleation can grow in all directions without any restrictions, leading naturally to a final spherical shape. The presence of blocking molecules, however, induces a selective and competitive condensation reaction at the terminals of the titanium hydroxide complexes, resulting in a cubic shape. Due to the complexity of the synthesis method, cubic TiO_2 has not yet been synthesized for application to DSSCs. Fortunately we were able to successfully obtain the cubic TiO_2 shape. After thermal treatment, the resulting precipitate is washed until the pH = 7.0 and then dried at 100 °C for 24 h.

2.2. Characterization of cubic TiO_2

The synthesized cubic TiO_2 powders were examined by XRD (Rigaku, D/MAX-1200) with nickel-filtered CuKα radiation (30 kV, 30 mA) at 2θ angles that ranged from 5° to 70° at scan speed of 10° min^{-1} and a time constant of 1 s. The sizes and shapes of the cubic TiO_2 particles were measured by high-resolution TEM (H-7600, Hitachi, Japan) operated at 120 kV.

Raman spectra were acquired using an RFS 100/S FT Raman spectrometer. The wavenumber values reported from the spectra were accurate to within 2.0 cm^{-1}. The emission line at 532 nm from the Argon-Laser (Nicolet Almega XR, Thermo Scientific, USA) was focused on the sample under a microscope and a ~1-μm diameter spot was analyzed. The power of the incident beam on the sample was 10 mW.

XPS (Cooperative Center to Research Facilities, Sungkyunkwan University Instrumental Analysis Center, Korea) measurements of

Ti2p and O1s were recorded with an ESCA 2000 (VZ MicroTech, Oxford, UK) system, equipped with a non-monochromatic AlK*a* (1486.6 eV) X-ray source. The base pressure of the ESCA system was below 1×10^{-9} Pa.

The reflectance UV–visible spectra were obtained using a Cary 500 spectrometer with a reflectance sphere over the spectral range of 200–800 nm. Samples of 1.0-mm pellets were measured at room temperature.

PL spectroscopy (Research Institute of Basic Sciences, Sunchon National University, Korea) was also performed to determine the number of photo-excited electron–hole pairs using a PL mapping system (LabRam HR, Sci-Tech Instruments), and to examine the number of photo-excited electron–hole pairs for all samples. Samples of 1.0-mm pellets were measured at room temperature using a He–Cd laser source at 325 nm in the reflection mode.

A.C. impedance measurements were performed with a potentiostat–galvanostat equipped with a CompactStat electrochemical interface from IVIUM technology under constant light illumination of 100 mW cm^{-2}. Impedance measurements were taken at frequencies between 0.1 and 100 kHz with an a.c. signal of 10 mV amplitude. The applied bias voltage and a.c. amplitude were set at the V_{oc} of the DSSCs. One sun illumination was obtained from a 100 W xenon lamp.

The surface states and electric properties of the TiO_2 film were determined by EFM analysis (resolution; 0.1 nm(*X*–*Y*), 0.01 nm (*Z*), Veeco Co.).

2.3. Manufacture of dye-sensitized solar cell (DSSC)

To prepare the cubic TiO_2 thin film, a slurry was produced by mixing 1.0 g of nano-sized, cubic TiO_2 powders with 10 mL of butyl alcohol solvent after sonication for 24 h at 1200 W. A TiO_2 film was fabricated by coating on to a fluorine-doped SnO_2 conducting glass plate (Hartford FTO, ~30 Ω cm^{-2}, 80% transmittance in visible region) using a squeeze printing technique (approximately 4.0 μm TiO_2 thickness). The film was treated by heating at 450 °C for 30 min to remove the alcoholic solvent. For DSSC manufacture, the prepared thin film electrode was immersed in a 3.0×10^{-4} M N719 dye solution at room temperature for 24 h, rinsed with anhydrous ethanol, and then dried. A Pt-coated FTO electrode was placed over the dye-adsorbed cubic TiO_2 electrode, and the edges of the cell were sealed with a sealing sheet (PECHM-1, Mitsui-DuPont Poly Chemical). The redox electrolyte consisted of 0.5 mol KI, 0.05 mol I_2, and 0.5 mol 4-tert-butylpyridine as a solvent. The photocurrent–voltage (*I*–*V*) curves were used to calculate the J_{sc}, V_{oc}, FF, and overall conversion efficiency of each DSSC. The *I*–*V* curves (ABET Technology, Sun2000 solar simulator) were measured under white light irradiation from a xenon lamp (max. 150 W, Newport). The incident light intensity and active cell area are 100 mW cm^{-2} and 0.42 (0.7 × 0.6) cm^2, respectively.

3. Results and discussion

3.1. Characteristics of cubic TiO_2

The HRTEM image (left) and selected area electron diffraction (SAED) pattern (right) of cubic TiO_2 and TEM images of the two TiO_2 particle shapes are shown in Fig. 2. The fringe spacing parallel to the nanocube is estimated to be 0.283 nm, which is close to the [1 0 1] lattice spacing of anatase TiO_2, and therefore indicates that the crystal growth occurs preferentially in the [1 0 1] direction. The electron diffraction pattern of the right image in Fig. 2A recorded on the regularly located nanocubes exhibits diffraction rings, thereby revealing that the nanocubes are polycrystalline and can be readily indexed as the TiO_2 phase. The relatively uniform mixture of rhombic and cubic particles exhibited in (a) of Fig. 2B, with sizes ranging from 10 to 20 nm, is a general form of TiO_2. When tetraethyl ammonium hydroxide is added as a blocking molecule, however, the particles completely form a cubic shape with the same size as shown in (b) and (c) in Fig. 2B.

The XRD patterns of the two types of TiO_2, namely, cubic and irregular spherical powders, are presented in Fig. 3. The TiO_2 particles have a pure anatase structure without being thermally treated above 500 °C. The anatase structure showed peaks at $2\theta = 25.3°$, 38.0°, 48.2°, 54°, 63° and 68°, which are assigned to the (d_{101}), (d_{004}), (d_{200}), (d_{105}), (d_{211}), and (d_{204}) planes, respectively [29]. Despite the different shapes, no peaks are assigned to impurities. The peak intensity at $2\theta = 25.3°$ assigned to the anatase [1 0 1] plane in pure TiO_2 increases significantly and is shifted downfield in the cubic TiO_2, compared with its spherical counterpart. This result is well matched to the HRTEM result shown in Fig. 2, in which the crystal is found to grow preferentially in the [1 0 1] direction. Additional peaks of [1 0 5] and [2 1 1] are completely divided in cubic TiO_2 compared with those for spherical TiO_2. These sharp edges are attributed to the depression of crystal growth. Scherrer's equation [30], $t = 0.9\lambda/\beta\cos\theta$, where λ is the wavelength of the incident X-rays, β the full width at half maximum height in radians, and θ the diffraction angle, was used to estimate the crystalline domain size. This value was 14 and 16 nm for spherical and cubic TiO_2, respectively.

For Raman spectroscopy, a laser was directed at the sample. The energy difference between the incident and reflected beams, usually measured in wavenumbers, corresponds to the change in molecular vibration within the sample. Characteristic bond vibrations allow identification of the chemical and crystal states of the sample. In particular, Raman spectroscopy has been extensively used to study the TiO_2 Td structure. The application of this technique here is valuable due to its ability to determine rapidly the surface crystal structure of TiO_2. Fig. 4 compares the Raman spectra of spherical and cubic TiO_2. Some researchers have investigated the Raman spectra of anatase TiO_2, and recorded the reference Raman spectra of the powders of TiO_2 Td structure (bonds at 639, 519, 513, 399, 197, and 144 cm^{-1}) [31,32]. In general, the band sharpness agrees well with the crystallinity. The primitive unit cell contains two TiO_2 Td formula units. Factor group analysis indicates the presence of optical modes with the following irreducible representation of normal vibrations: $1A_{1g} + A_{2u} + 2B_{1g} + 1B_{2u} + 3E_g + 3E_u$. The modes of A_{1g}, B_{1g}, and E_g are Raman active, whereas those of A_{2u} and E_u are infrared active. In Fig. 4, cubic TiO_2 exhibits sharper special bands than the spherical version. In particular, the band of E_g at 144 cm^{-1} is shifted downfield, and this is attributed to crystal growth in the [1 0 1] plane and agrees well with XRD analysis.

Typical high-resolution, quantitative XPS spectra of spherical and cubic TiO_2 are presented in Fig. 5. The survey spectra of the particles contain Ti2p and O1s peaks. The $Ti2p_{1/2}$ and $Ti2p_{3/2}$ spin-orbital splitting photoelectrons for the two samples are located at the binding energies of 464 and 458 eV [33,34], respectively. In general, a large binding energy indicates a more oxidized state. For cubic TiO_2, the curves are slightly shifted to a lower binding energy, indicating that the Ti oxidation state is slightly changed by the crystal morphology and, hence, that the Ti–O bonding strength is weaker in cubic TiO_2 according to the hard soft acid base (HSAB) rule, thereby resulting in easier electron flow. Generally, the O1s region consists of several contributions. The main contributions are attributed to Ti–O (529.0 eV), Ti–OH (hydroxyl group, 532.0 eV), and adsorbed H_2O (534.0 eV) in TiO_2. The Gaussian values are used in the curve resolution of the individual O1s peaks. The only spectrum observed in cubic TiO_2 is the first peak at 529.5 eV, which is assigned to Ti–O. The spherical shape, however, has an additional second peak at 532.0 eV, which is assigned to Ti–OH. As in Ti2p, the O1s peak is also shifted to a lower binding energy in cubic TiO_2.

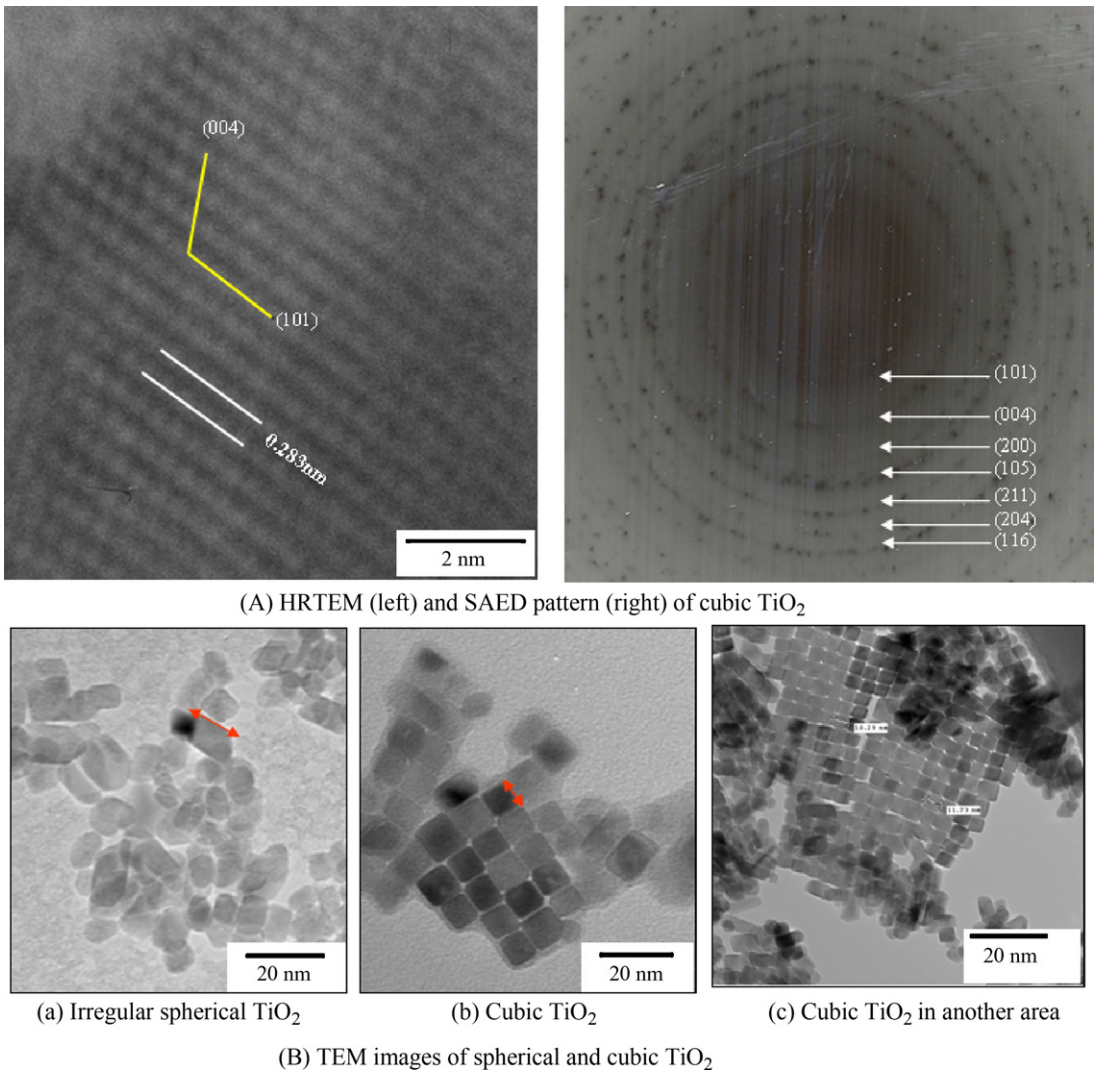

Fig. 2. TEM images of spherical and cubic TiO_2: (A) HRTEM image (left) and SAED pattern (right) of cubic TiO_2; (B) TEM images of spherical and cubic TiO_2.

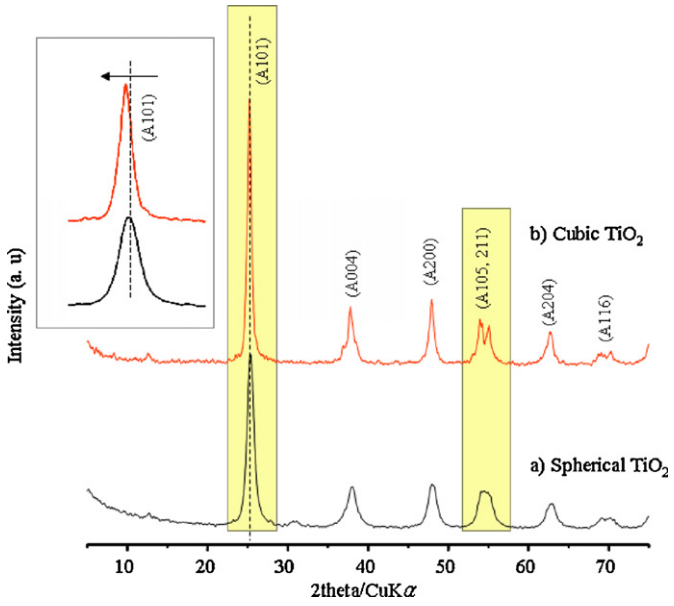

Fig. 3. XRD patterns of spherical and cubic TiO_2.

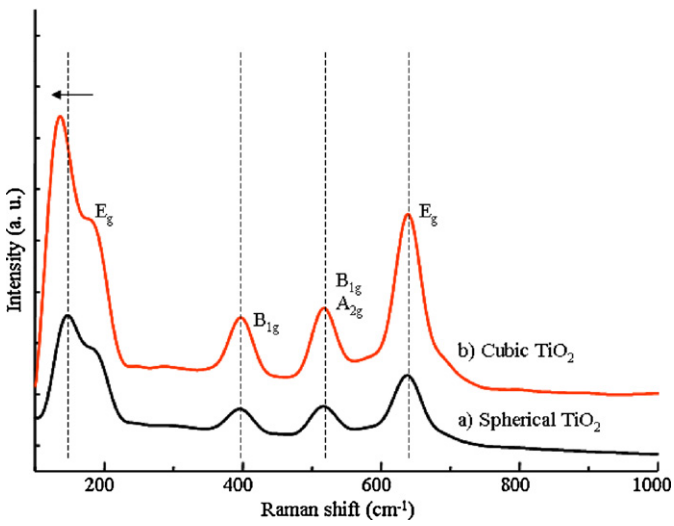

Fig. 4. FT-Raman spectra of spherical and cubic TiO_2.

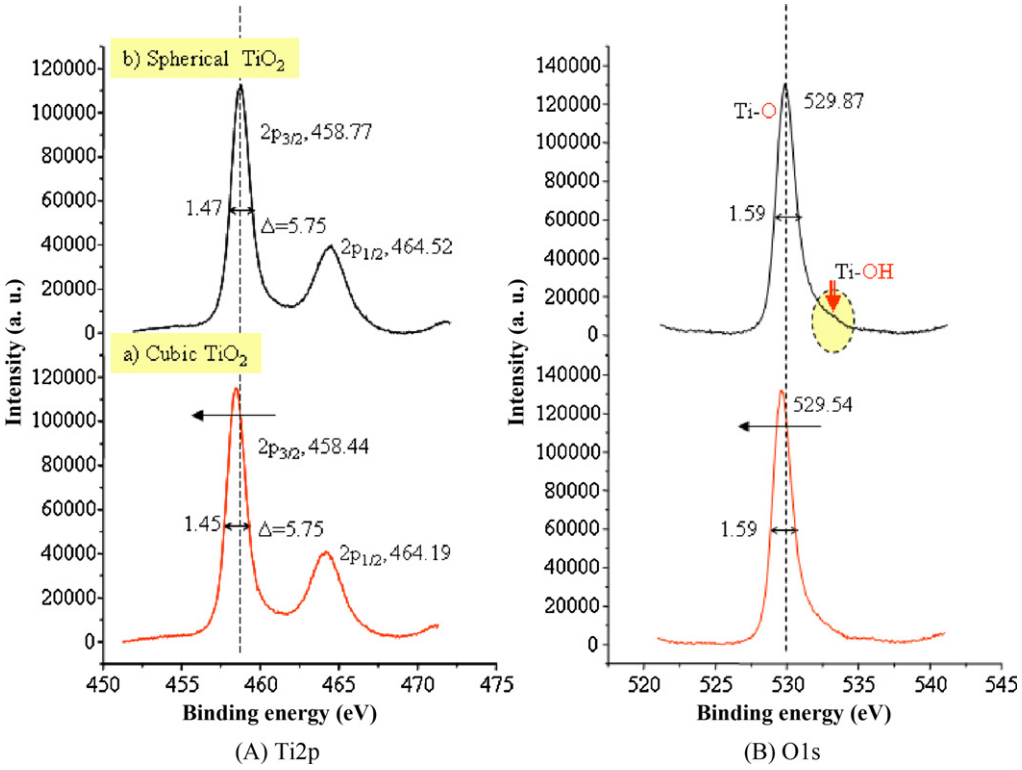

Fig. 5. XPS spectra of spherical and cubic TiO_2.

3.2. Photovoltaic performance of cubic TiO_2

The photoelectric properties were measured using a voltmeter and ampere meter (Model 2000, Keithley) with a variable load. A 150-W illuminant Xenon lamp was employed as a radiation source at an AM-1.5 radiation angle. The light intensities are measured using a power analyzer and a thermal smart-sensor. The FF and solar energy conversion efficiency (η) are calculated by Eqs. (1) and (2), respectively [35,36].

$$\mathrm{FF} = \frac{I_{\max} \times V_{\max}}{I_{sc} \times V_{oc}} \quad (1)$$

$$\eta\ (\%) = \frac{P_{out}}{P_{in}} \times 100 = I_{\max} \times \frac{V_{\max}}{P_{in}} \times 100 = I_{sc} \times V_{oc} \times \mathrm{FF} \quad (2)$$

The *I*–*V* curves of the two TiO_2 particle shapes synthesized using a hydrothermal method are given in Fig. 6. The film depth is close to 4.0 μm, as shown in the right photo. The FF, V_{oc}, J_{sc}, and overall energy efficiency are determined using the equations shown above. A DSSC assembled with spherical TiO_2 exhibited a V_{oc} of 0.70 and a J_{sc} of 15.84 mA cm^{-2}. The power conversion efficiency of the spherical TiO_2 anatase structure (6.0-μm film thickness) is 7.09%, compared with 9.77% in the DSSC made from the cubic TiO_2 film, with a J_{sc} density of 20.83 mA cm^{-2}. This result confirmed the superiority of cubic TiO_2 over spherical TiO_2 for application as a DSSC material.

3.3. Optical properties of cubic TiO_2

The UV–visible spectra of the two TiO_2 particle shapes were obtained to determine the relationship between the solar energy conversion efficiency and the spectroscopic property, as shown in Fig. 7A. The absorption band for the tetrahedral symmetry of Ti^{4+} normally appears at approximately 350–380 nm, and is assigned to ligand (p-orbital) to metal (d-orbital) charge transfer. The band gaps in a semiconductor material are closely related to the wavelength range absorbed, where the band gap decreases with increasing absorption wavelength. The absorption bands are slightly larger in spherical TiO_2 than in cubic TiO_2. A remarkable feature is the broadened tail in the cubic TiO_2, due to d (T2g)–d (Eg) transfer when an electron exists in the d-orbital of Ti^{3+}. Fig. 7B shows the PL spectra of the two TiO_2 particle shapes. The curve suggests that the electrons in the valence band are transferred to the conduction band, after which the excited electrons are stabilized by photoemission. In general, the PL intensity increases with increasing number of emitted electrons resulting from recombination between excited electrons and holes, and a consequent decrease in photoactivity [37,38]. Therefore, there is a strong relationship between the PL intensity and photoactivity. In particular, the PL intensity decreases to a greater extent when a metal can capture excited electrons or exhibit conductivity, which is known as the relaxation process. The PL curves of the two TiO_2 particle shapes exhibit yellow emission at 565 nm. The band broadening is attributed to the overlapped emission from the higher and lower excited states to the ground states. The PL intensity decreases significantly in cubic TiO_2, due to the effect of its clean surface in facilitating electron transfer and hence depressing the recombination process. Consequently, easier electron transfer activities are expected on the surface of cubic TiO_2.

All the impedance spectra shown in Fig. 8 illustrated three semicircles in the measured frequency range of 0.1–100 kHz. Notably, Rs, the ohmic serial resistance, is associated with the series resistance of the electrolytes and electric contacts in the DSSCs. R1, the charge-transfer resistance, occurs at the Pt counter electrode. R2 and R3 have been associated with the resistance at the TiO_2|dye|electrolyte interface and the Nernstian diffusion within the electrolytes, respectively [39,40]. All the measured impedance data for the two types DSSCs are also included in the Table below Fig. 8 and the values are adjusted to a zero value for Rs. Spherical TiO_2-DSSC appears to exhibit a total resistance in the current path

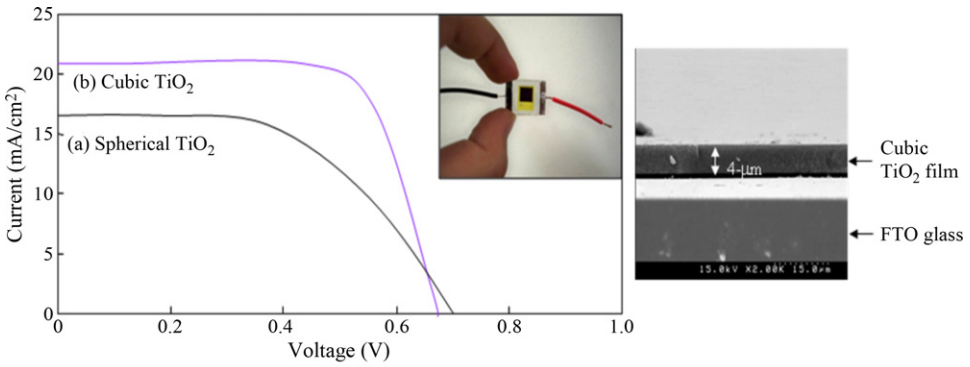

Working electrode	Dye	Efficiency (%)	Fill factor	Voc	Jsc
Cubic TiO_2	N719	9.77	0.70	0.67	20.83
Spherical TiO_2	N719	7.09	0.64	0.70	15.84

Fig. 6. Solar energy conversion efficiency of DSSCs fabricated with spherical and cubic TiO_2 and film thickness of cubic TiO_2.

across the device that is higher than in the cubic TiO_2-DSSC. In addition, the trend of changes for Rs is the same in both DSSCs, whereas R1, R2 and R3 vary greatly between the two types of DSSC. Notably, R_2, which is the resistance at the TiO_2|dye|electrolyte interface, is markedly more decreased in a cell that is assembled with cubic TiO_2 than with spherical TiO_2. This confirms the ease of electron transfer over the surface of TiO_2, the increased electron flow and, therefore, the enhanced photocurrent and powder efficiency of the DSSC with cubic TiO_2.

The analytical EFM method was used to determine whether a flat electrode surface improves the electron mobility. Typically, the presence of a conductor and non-conductor within a nano-leveled film in the visual image can be distinguished by atomic force microscopy (AFM) using the modified EFM image. The power

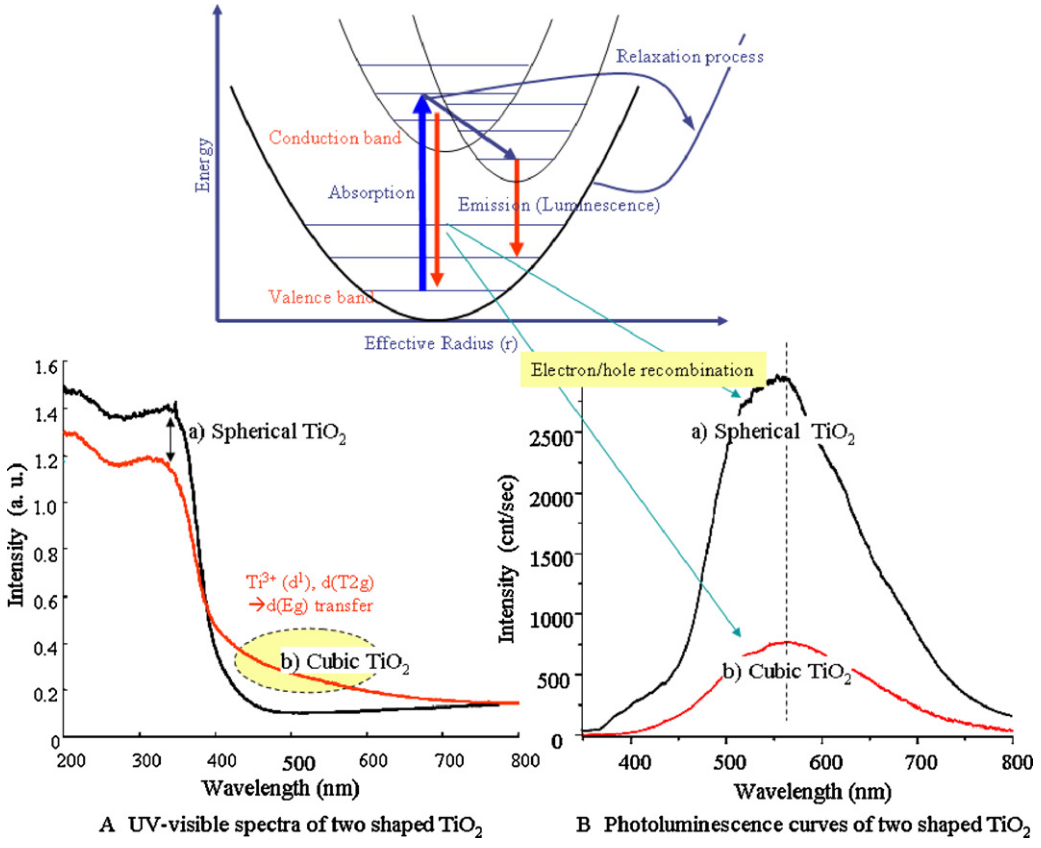

Fig. 7. UV–visible and PL spectra of spherical and cubic TiO_2: (A) UV–visible spectra and (B) PL curves of two TiO_2 particle shapes.

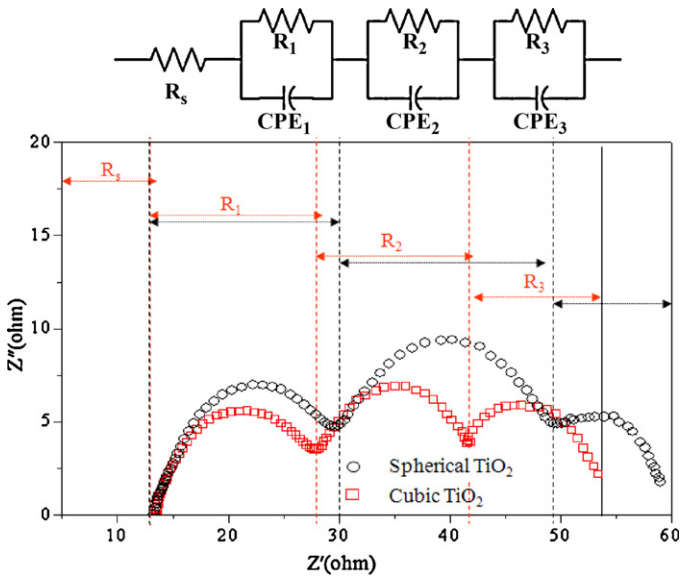

	R_1	R_2	R_3
Spherical TiO_2	16.31	20.50	8.85
Cubic TiO_2	14.55	13.54	11.85

Fig. 8. Electrochemical impedance spectra of DSSCs assembled with spherical and cubic TiO_2.

strength between the samples is measured while traversing the voltage to the AFM tip bias. The presence of conducting and non-conducting areas in the sample can be determined from the responses of the AFM tip [41]. The phase changes periodically with the tip vibrating power cycle (charge, magnetic, etc.). Consequently, the differences between the conducting and non-conducting surfaces are indicated by the amplitude and phase changes, and the change in width is expressed as the contrast of the average surface roughness (Ra) values indicated in the image. This value in the phase is represented by the electrostatic field gradient. Therefore, the Ra value increases markedly when tips with specific current paths are used. The Ra value can be determined indirectly by changing the tip, and directly by next Eq. (3) [42,43]. Here, $f(x, y)$ is the surface relative to the center plane, and L_x and L_y are the dimensions of the surface.

$$\mathrm{Ra} = \frac{1}{L_x L_y} \int_0^{L_x} \int_0^{L_y} \left| f(x, y) \right| \, dx \, dy \tag{3}$$

The EFM images of the two TiO_2 particle shape films with a N719 dye in darkroom (B) and light (C) conditions are shown in Fig. 9. At a voltage of 3.0 eV and a film thickness of 2.0 μm, the phase change does not exceed a maximum of 3.0° in either sample. The phase difference is the difference in electrostatic force between the phases, thereby inducing the phase brightness [44]. Generally a bright image indicates the charge flow. The brightness is increased under light conditions in both samples compared with that found in a darkroom. The cubic TiO_2 film shows a more significant result under light conditions than does spherical TiO_2. The Table at the

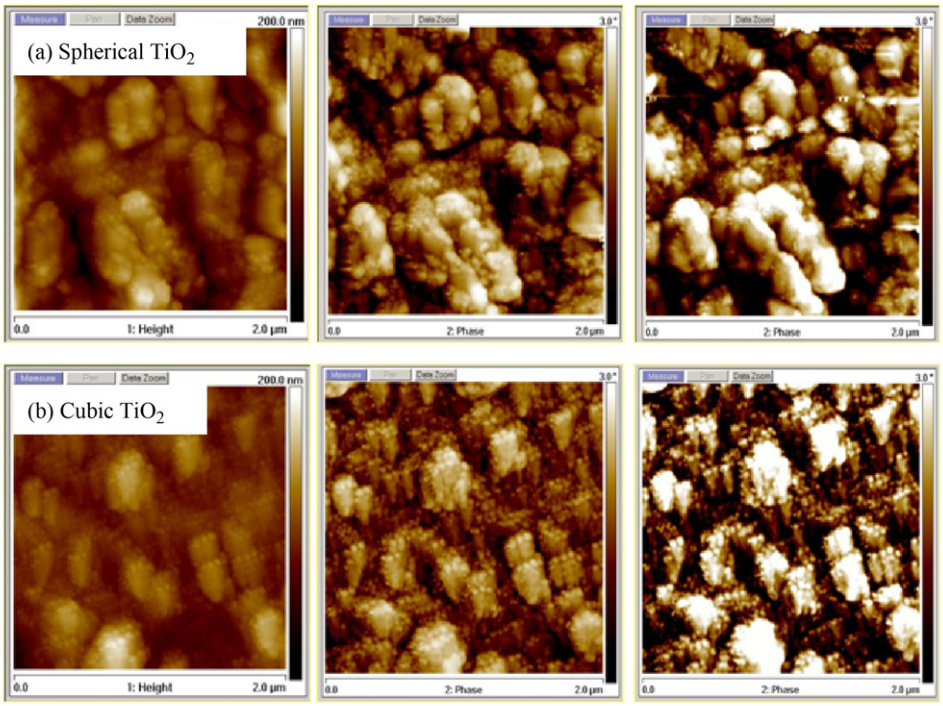

(A) AFM (B) EFM under dark condition (C) EFM under light condition

Sample	Darkroom (Ra)	under the light (Ra)	Ra-gap
Spherical TiO_2	0.546°	0.836°	0.290°
Cubic TiO_2	0.410°	0.874°	0.464°

Fig. 9. Images of AFM and EFM analyses of spherical and cubic TiO_2 under dark and light conditions: (A) AFM, (B) EFM under dark condition, and (C) EFM under light condition.

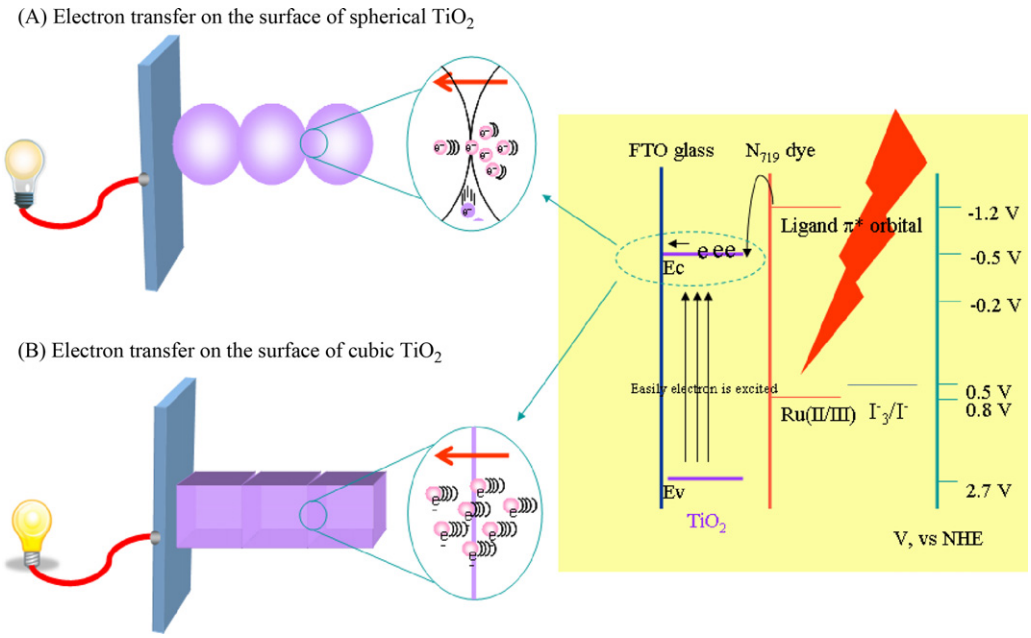

Fig. 10. Expectation models of electron transfer on surface of (A) spherical and (B) cubic TiO_2.

bottom of the Fig. 9 lists the Ra values of the two TiO_2 particle shape films upon dye absorption in the darkroom and in the light. The cubic TiO_2/dye film does not differ significantly from the spherical TiO_2/dye film under dark conditions, but has a Ra value that is 0.464° higher than that found under light conditions. This confirms the high mobility of the electrons flowing on the surface of the cubic TiO_2 film.

4. Conclusions

The key achievement of this study is the successful synthesis of cubic TiO_2. Based on the characteristics, of this material, two models are suggested in Fig. 10 to explain the effect of the morphological shape of anatase on the high-energy conversion efficiency. EFM and cell impedance analyses reveal that a flat TiO_2 surface with a cubic shape can easily donate electrons received from the LUMO of the dye molecules to the FTO electrode. Fig. 10B shows the energy levels of all DSSC compositions. The light absorbed by a dye molecule excites the electrons in the HOMO to an electronically excited state, LUMO, after which they were transferred to the conduction band of TiO_2 and finally to the conducting electrode of FTO glass. On the spherical TiO_2 surface shown in Fig. 10A, the passage of electrons received from the dye molecules through the surface is assumed to be difficult, thereby decreasing the number of transferred electrons and reducing the photovoltaic efficiency. On the other hand, the flat surface of cubic TiO_2 shown in Fig. 10B enables the electrons received from the dye molecules to pass easily through the surface, which increases the number of transferred electrons because the photovoltaic efficiency improves due to the absence of any electron loss. These results confirm the importance of the crystal morphology for smooth electron movement and the potential to improve the photon conversion efficiency in DSSCs by controlling this morphology.

Acknowledgements

This work was supported by the Basic Science Research Program through the National Research Foundation of Korea (NRF) funded by the Ministry of Education, Science and Technology (KRF-2008-313-D00222), for which the authors are very grateful.

References

[1] J.M. Kroon, N.J. Bakker, H.J.P. Smit, P. Liska, K.R. Thampi, P. Wang, S.M. Zakeeruddin, M. Graetzel, A. Hinsch, S. Hore, U. Würfel, R. Sastrawan, J.R. Durrant, E. Palomares, H. Pettersson, T. Gruszecki, J. Walter, K. Skupien, G.E. Tulloch, Prog. Photovolt. Res. Appl. 15 (2007) 1–18.
[2] M. Graetzel, J. Photochem. Photobiol. A 164 (2004) 3–14.
[3] M. Graetzel, Inorg. Chem. 44 (2005) 6841–6851.
[4] M. Späth, P.M. Sommeling, J.A.M. van Roosmalen, H.J.P. Smit, N.P.G. van der Burg, D.R. Mahieu, N.J. Bakker, J.M. Kroon, Prog. Photovolt. Res. Appl. 11 (2003) 207–220.
[5] W.J. Lee, E. Ramasamy, D.Y. Lee, J.S. Song, Sol. Energy Mater. Sol. Cells 91 (2007) 1676–1680.
[6] B. O'Regan, M. Graetzel, Nature 353 (1991) 737–739.
[7] F.L Qiu, A.C. Fisher, A.B. Walker, L.M. Peter, Electrochem. Commun. 5 (2003) 711–716.
[8] T.-V. Nguyen, H.-C. Lee, O.-B. Yang, Sol. Energy Mater. Sol. Cells 90 (2006) 967–981.
[9] H.-J. Koo, J. Park, B. Yoo, K. Yoo, K. Kim, N.-G. Park, Inorgan. Chim. Acta 36 (2008) 677–683.
[10] M. Dürr, A. Schmid, M. Obermaier, S. Rosselli, A. Yasuda, G. Nelles, Nat. Mater. 4 (2005) 607–611.
[11] X. Tang, J. Qian, Z. Wang, H. Wang, Q. Feng, G. Liu, J. Colloid Interface Sci. 330 (2009) 386–391.
[12] K.H. Ko, Y.C. Lee, Y.J. Jung, J. Colloid Interface Sci. 283 (2005) 482–487.
[13] P. Hasin, M.A. Alpuche-Aviles, Y. Li, Y. Wu, J. Phys. Chem. C 13 (2009) 7456–7460.
[14] P.V. Kamat, J. Phys. Chem. C 111 (2007) 2834–2860.
[15] W. Chen, X. Sun, Q. Cai, D. Weng, H. Li, Electrochem. Commum. 9 (2007) 382–385.
[16] U. Bach, D. Lupo, P. Comte, J.E. Moser, F. Weissärtel, J. Salbeck, H. Spreitzer, M. Grätzel, Nature 395 (1998) 583–589.
[17] M. Zukalova, A. Zukal, L. Kavan, M.K. Nazeeruddin, P. Liska, M. Graetzel, Nano Lett. 5 (2005) 1789–1792.
[18] B.-Q. Liu, X.-P. Zhao, W. Luo, Dyes Pigments 76 (2008) 327–331.
[19] C.-J. Lin, W.-Y. Yu, S.-H. Chien, Appl. Phys. Lett. 93 (2008) 133107-3.
[20] A.B.F. Martinson, J.W. Elam, J.T. Hupp, M.J. Pellin, Nano Lett. 7 (2007) 2183–2187.
[21] S. Chappel, S.-G. Chen, A. Zaban, Langmuir 18 (2002) 3336–3342.
[22] J. Wu, S. Hao, J. Lin, M. Huang, Y. Huang, Z. Lan, P. Li, Cryst. Growth Des. 8 (2008) 247–252.
[23] K.-M. Lee, V. Suryanarayanan, J.-H. Huang, K.R.J. Thomas, J.T. Lind, Kuo-Chuan Ho, Electrochim. Acta 54 (2009) 4123–4130.
[24] K.H. Park, C.K. Hong, Electrochem. Commun. 10 (2008) 1187–1190.
[25] K.-M. Lee, V. Suryanarayananb, K.-C. Ho, J. Power Sources 188 (2009) 635–641.
[26] Y. Zhang, L. Wu, E. Xie, H. Duan, W. Han, J. Zhao, J. Power Sources 189 (2009) 1256–1263.
[27] Y. Lee, Y. Kim, H. Jeong, M. Kang, J. Ind. Eng. Chem. 14 (2008) 655–660.
[28] J.H. Lee, W. Nam, M. Kang, G.Y. Han, K.J. Yoon, M.-S. Kim, K. Ogino, S. Miyata, S.-J. Choung, Appl. Catal. A 244 (2009) 49–57.
[29] Y. Dai, C.M. Cobley, J. Zeng, Y. Sun, Y. Xia, Nano Lett. 9 (2009) 2455–2459.
[30] T. Bezrodna, G. Puchkovska, V. Shymanovska, A. Hauser, J. Phys. Chem. Solids 66 (2005) 1057–1063.

[31] D. Wang, J. Zhao, B. Chen, C. Zhu, J. Phys. Condens. Mater. 20 (2008) 0852127 (p7).
[32] W.F. Zhang, Y.L. He, M.S. Zhang, Z. Yin, Q. Chen, Phys. D: Appl. Phys. 33 (2000) 912–916.
[33] S. Pétigny, H. Mostéfa-Sba, B. Domenichini, E. Lesniewska, A. Steinbrunn, S. Bourgeois, Surf. Sci. 410 (1998) 250–257.
[34] P. Le Fe'vre, J. Danger, H. Magnan, D. Chandesris, J. Jupille, S. Bourgeois, M.-A. Arrio, R. Gotter, A. Verdini, A. Morgante, Phys. Rev. B 69 (2004) 155421-9.
[35] M. Graetzel, J. Photochem. Photobiol. C 4 (2003) 145–153.
[36] K. Kalyanasundaram, M. Graetzel, Coord. Chem. Rev. 77 (1998) 347–414.
[37] J. Chae, J. Lee, J. Jeong, M. Kang, Bull. Korean Chem. Soc. 30 (2009) 302–308.
[38] B.S. Kwak, J. Chae, J. Kim, M. Kang, Bull. Korean Chem. Soc. 30 (2009) 1047–1053.
[39] F. Fabregat-Santiagoa, J. Bisquert, E. Palomares, S.A. Haque, J.R. Durrant, J. Appl. Phys. 100 (2006) 034510-7.
[40] C.-W. Tu, K.-Y. Liu, A.-T. Chien, C.-H. Lee, K.-C. Ho, K.-F. Lin, Eur. Polym. J. 44 (2008) 608–614.
[41] F.M. Serry, K. Kjoller, J.T. Thornton, R.J. Tench, D. Cook, Electric Force Microscopy, Surface Potential Imaging, and Surface Electric Modification with the Atomic Force Microscope, Veeco Instruments Inc., 2007.
[42] T.V. Vorburger, J.A. Dagata, G. Wilkening, K. Lizuka, in: Czandernal, et al. (Eds.), Characterization of Surface Topography, Beam Effects, and Depth Profiling in Surface Analysis, Plenum Press, New York, 1998.
[43] H.-T. Sun, Z.-H. Li, J. Zhou, Y.-Y. Zhao, M. Lu, Appl. Surf. Sci. 253 (2007) 6109–6112.
[44] P. Girard, Nanotechnology 12 (2001) 485–490.